The Astrophysical Journal Letters, 891:L23 (7pp), 2020 March 1 https://doi.org/10.3847/2041-8213/ab7825

The Blue Compact Dwarf Galaxy VCC 848 Formed by Dwarf–Dwarf Merging

Hong-Xin Zhang[1,2], Sanjaya Paudel[3], Rory Smith[4], Pierre-Alain Duc[5], Thomas H. Puzia[6], Eric W. Peng[7,8], Patrick Côte[9], Laura Ferrarese[9], Alessandro Boselli[10], Kaixiang Wang[7,8], and Se-Heon Oh[11]
[1] CAS Key Laboratory for Research in Galaxies and Cosmology, Department of Astronomy, University of Science and Technology of China, Hefei, Anhui 230026, People's Republic of China; hzhang18@ustc.edu.cn
[2] School of Astronomy and Space Science, University of Science and Technology of China, Hefei 230026, People's Republic of China
[3] Department of Astronomy and Center for Galaxy Evolution Research, Yonsei University, Seoul 03722, Republic of Korea; sanjpaudel@gmail.com
[4] Korea Astronomy and Space Science Institute, Daejeon 305-348, Republic of Korea; rorysmith@kasi.re.kr
[5] Université de Strasbourg, CNRS, Observatoire astronomique de Strasbourg, UMR 7550, F-67000 Strasbourg, France
[6] Instituto de Astrofísica, Pontificia Universidad Católica de Chile, 7820436 Macul, Santiago, Chile
[7] Department of Astronomy, Peking University, Beijing 100871, People's Republic of China
[8] Kavli Institute for Astronomy and Astrophysics, Peking University, Beijing 100871, People's Republic of China
[9] National Research Council of Canada, Herzberg Astronomy and Astrophysics Program, 5071 West Saanich Road, Victoria, BC V9E 2E7, Canada
[10] Aix Marseille Université, CNRS, LAM (Laboratoire d'Astrophysique de Marseille) UMR 7326, F-13388 Marseille, France
[11] Department of Physics and Astronomy, Sejong University, 209 Neungdong-ro, Gwangjin-gu, Seoul, Republic of Korea
Received 2020 February 4; revised 2020 February 19; accepted 2020 February 19; published 2020 March 4

Abstract

It has long been speculated that many starburst or compact dwarf galaxies are resulted from dwarf–dwarf galaxy merging, but unequivocal evidence for this possibility has rarely been reported in the literature. We present the first study of deep optical broadband images of a gas-dominated blue compact dwarf galaxy (BCD) VCC 848 ($M_\star \simeq 2 \times 10^8 M_\odot$) that hosts extended stellar shells and thus is confirmed to be a dwarf–dwarf merger. VCC 848 is located in the outskirts of the Virgo Cluster. By analyzing the stellar light distribution, we found that VCC 848 is the result of a merging between two dwarf galaxies with a primary-to-secondary mass ratio $\lesssim$5 for the stellar components and $\lesssim$2 for the presumed dark matter halos. The secondary progenitor galaxy has been almost entirely disrupted. The age–mass distribution of photometrically selected star cluster candidates in VCC 848 implies that the cluster formation rate (CFR, $\propto$ star formation rate) was enhanced by a factor of $\sim$7–10 during the past $\sim$1 Gyr. The merging-induced enhancement of CFR peaked near the galactic center a few hundred Myr ago and has started declining in the last few tens of Myr. The current star formation activities, as traced by the youngest clusters, mainly occur at large galactocentric distances ($\gtrsim$1 kpc). The fact that VCC 848 is still (atomic) gas-dominated after the period of the most violent collision suggests that gas-rich dwarf galaxy merging can result in BCD-like remnants with extended atomic gas distribution surrounding a blue compact center, in general agreement with previous numerical simulations.

Unified Astronomy Thesaurus concepts: Dwarf galaxies (416); Dwarf irregular galaxies (417); Galaxies (573); Galaxy pairs (610); Interacting galaxies (802); Irregular galaxies (864); Late-type galaxies (907); Starburst galaxies (1570); Amorphous irregular galaxies (37); Blue compact dwarf galaxies (165); Galaxy evolution (594); N galaxies (1084)

1. Introduction

Galaxy mergers, especially those involving gas-rich comparable-mass galaxies, can dramatically change galaxy morphologies, enhance star formation activities, and trigger active galactic nuclei in short timescales (Naab & Ostriker 2017 and references therein). The majority of studies of galaxy mergers so far have focused on relatively massive galaxies, while mergers between dwarf galaxies ($M_\star < 10^9$) received little attention until very recently. In contrast to their massive counterparts, star-forming dwarf galaxies, and hence their mergers, are often gas dominated. Relative proportions of the dissipative gas component and the nondissipative stellar component can make substantial differences to the merging process.

The first solid evidence for a dwarf–dwarf merger was found in the dwarf spheroidal galaxy Andromeda II by Amorisco et al. (2014). Since then (see, however, Chilingarian 2009), signatures of past merger events have been reported in several early-type dwarf galaxies (Paudel et al. 2017; Cicuendez & Battaglia 2018). Stierwalt et al. (2015) carried out the first systematic study of gas-rich dwarf–dwarf interacting pairs and found that the star formation rate (SFR) of relatively close pairs is enhanced by a factor of $\sim$2 on average. Pearson et al. (2016) further showed that gas-rich dwarf pairs have more extended atomic gas distribution than unpaired analogs. In addition, case studies of several more star-forming dwarf pairs have been carried out recently (Annibali et al. 2016; Paudel & Sengupta 2017; Privon et al. 2017; Makarova et al. 2018; Paudel et al. 2018a, 2018b; Johnston et al. 2019).

Previous studies of gas-rich dwarf–dwarf interactions are biased toward well-separated pairs, which is partly due to the difficulty in identifying merging signatures from morphologically irregular dwarf galaxies in general. It remains to be seen how a dwarf–dwarf merger impacts the overall star formation activities and morphology of merger remnants. Here we present a study of a unique blue compact dwarf galaxy (BCD), VCC 848 ($M_B = -16.05$ mag; Gil de Paz et al. 2003), which stands out with faint but remarkably extended stellar shells wrapping around the stellar main body.[12] Stellar shells are unambiguous

[12] After a systematic search for fine substructures in Virgo star-forming dwarfs, we found several more Virgo BCDs ($\sim$25%) with hints of tidal shells, but they are not as impressive as those in VCC 848.

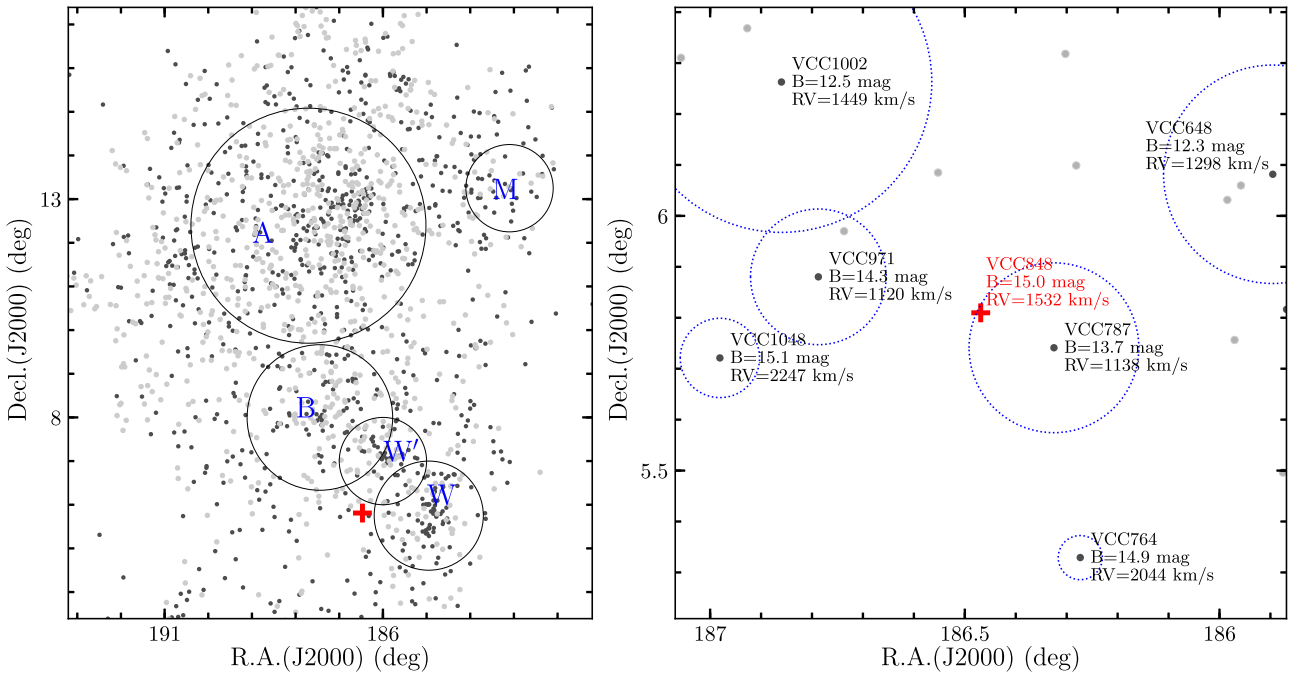

Figure 1. Location of VCC 848 in the sky area of the Virgo cluster. The left panel presents the spatial distribution of redshift-confirmed (black symbols) or candidate (gray dots) VCC galaxies (Binggeli et al. 1985) according to the most recent compilation of redshift measurements by the NGVS team. The red plus symbol marks the location of VCC 848. The two biggest black solid circles mark half the virial radius of M87 (A) and of M49 (B) subclusters, respectively, and the three small black solid circles mark the boundaries of the M, W′, and W clouds, as defined in Binggeli et al. (1987). The right panel is a zoom-in of the $1.^{\circ}2 \times 1.^{\circ}2$ sky area around VCC 848. The blue dotted circles in the right panel mark half the virial radii of individual confirmed VCC galaxies, where the virial radius is approximated as the *i*-band half-light radius times 67 (Kravtsov 2013).

signatures of minor or major galaxy merger events in the recent past (e.g., Hernquist & Quinn 1988; Hernquist & Spergel 1992), but have not been reported for star-forming dwarfs previously.

VCC 848 (R.A. = $186.^{\circ}46853$, decl. = $5.^{\circ}80930$) is located in the outskirts of the Virgo cluster. As illustrated in Figure 1, it is $6.^{\circ}7$ ($\simeq$1.9 Mpc in projection) away from the Virgo central galaxy M87 and $2.^{\circ}4$ ($\simeq$0.7 Mpc in projection) away from the dominant galaxy M49 of the Virgo B subcluster, and it is also outside of the boundaries of other Virgo substructures. It has a radial velocity of 1532 km s^{-1}, which can be compared to $\sim$1000 km s^{-1} of the Virgo B subcluster. Furthermore, VCC 848 is virtually free of gravitational influence from its neighboring galaxies, given its current location and radial velocity. VCC 848 is rich in neutral H I gas (M(H I) = $4.2 \times 10^8 M_{\odot}$; Haynes et al. 2011), with M(H I)/$L_B \simeq 1.0\ M_{\odot}/L_{\odot}$, and has an H I deficiency parameter of -0.2 (Grossi et al. 2015), which means that its H I gas mass is 0.2 dex higher than that expected for isolated galaxies of similar Hubble types and sizes (Haynes & Giovanelli 1984). By using the SFR estimator from Catalan-Torrecilla et al. (2015), the current SFR of VCC 848 is estimated to be 0.023 $M_{\odot}$ yr^{-1} based on the Hα image from Gil de Paz et al. (2003) and *Herschel* far-infrared photometry from Grossi et al. (2015). According to the SFR −stellar mass relation (Shin et al. 2019), VCC 848 is 0.19 dex above the star formation main sequence for its stellar mass ($2 \times 10^8\ M_{\odot}$; see Section 3.3).

This Letter aims to exploit the broadband imaging data of VCC 848 to investigate the impact of merging on the stellar distribution and star formation history (SFH). In Section 2, we describe the data used in this work. In Section 3, we present the stellar light distribution and isophotal analysis. In Section 4, we present the detection of star cluster candidates and its implications for the past SFH. A summary is given in Section 5. Throughout this Letter, the Schlafly & Finkbeiner (2011) Galactic extinction map is used to correct our photometry and a distance of 16.5 Mpc is adopted for VCC 848 (Blakeslee et al. 2009).

2. Broadband Optical Imaging Data

Broadband *u*-, *g*-, *i*-, *z*-band images of VCC 848 were obtained with the MegaCam instrument on the Canada–France–Hawaii Telescope. The observations are part of the Next Generation Virgo Cluster Survey (NGVS; Ferrarese et al. 2012), which reaches a 2σ surface brightness limit of $\mu_g \simeq 29$ mag arcsec^{-2}. The processed NGVS images for the VCC 848 field have $0.''186$ pixel scales and point-spread function FWHMs of $0.''78$, $0.''71$, $0.''53$, and $0.''62$ respectively for *u*, *g*, *i*, and *z* passbands.

3. Stellar Light Distribution

3.1. Description of the Tidal Features

In order to better visualize faint substructures, we mask out bright foreground stars or background galaxies in the *g* image, and then use the adaptive smoothing code ADAPTSMOOTH (Zibetti et al. 2009) to adaptively smooth the masked *g*-band image to a minimum signal-to-noise ratio (S/N) of 5 pixel^{-1}. The smoothed image is shown in Figure 2. One can notice three extended shell-like structures around the bright stellar main body. These shell structures are largely aligned along the east–west direction, and the innermost one is brighter and has sharper edges than the two at larger radii. Moving toward smaller radii, there is a circularly edged stream-like feature wrapping nearly 180° around the stellar main body to the southeast. Last, there is a straight stream-like narrow feature

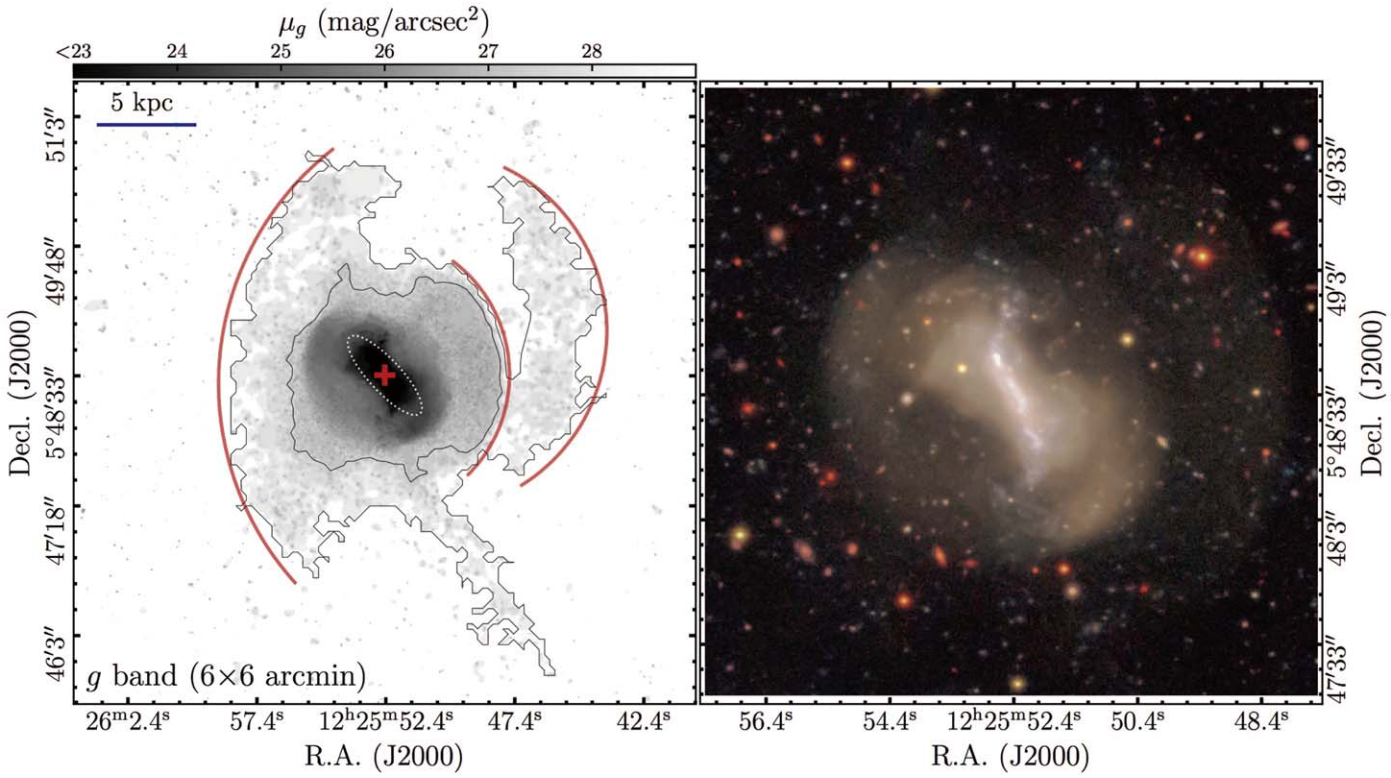

Figure 2. Left: *g*-band image of VCC 848. The original NGVS image has been adaptively smoothed to a minimum S/N of 5. The two contour levels mark, respectively, surface brightnesses of 27.3 and 28.3 mag arcsec^{-2}. The three most obvious sharp-edged shell-like structures are marked by orange curves. The photometric center of VCC 848 is marked by a red plus symbol. The white dotted ellipse has $R_{\rm maj} = 30''$ and encloses the stellar main body dominated by the primary progenitor of the merger. Right: central $2\farcm5 \times 2\farcm5$ of the *u, g, i* color composite image.

that extends to the southwest and is largely parallel to the orientation of the stellar main body.

3.2. Isophotal Analysis

To quantify the stellar light distribution, we perform surface photometry in the original *g*- and *i*-band images with the IRAF task ELLIPSE. Our isophotal fitting is carried out in an iterative manner in order to find the photometric center, which is constant with radius, and the ellipticity and position angle (PA) that vary with radius. The results are shown in Figure 3.

The stellar main body of VCC 848 has twisted isophotes, with the PA varying from $\simeq 32°$ near the center to 42° at a major axis radius $R_{\rm maj} \simeq 28''$ ($\sim$2.2 kpc) where boxy distortion of the isophotes reaches the maximum (ELLIPSE B4 coefficient $\simeq -0.3$; bottom right panel of Figure 3). Beyond the central $\sim 30''$ (i.e., the stellar main body) are the above-described tidal streams and shells, which apparently drive the abrupt decrease of isophotal ellipticities at large radii ($R_{\rm maj} \gtrsim 40''$). Photometry integrated over the area enclosed by the 27.3 and 28.3 mag arcsec^{-2} *g*-band brightness contours is shown as red open square symbols in Figure 3.

The $(g-i)$ colors become redder at larger radii. The obscured star formation traced by *Herschel* far-infrared photometry accounts for merely 9% of the SFR budget of VCC 848 (Section 1). So the radial color trend primarily reflects an increasingly older stellar population toward larger radii. The shell-dominated region reaches $g-i \simeq 0.6$–0.7 mag that, for single stellar populations (SSPs) at one-fifth solar metallicity (i.e., the nebular gas abundance measured by Vilchez & Iglesias-Paramo 2003), would correspond to stellar ages of 2–3 Gyr.

3.3. Implications for the Primary-to-secondary Mass Ratio and Collision Geometry

The radial surface brightness distribution at $R_{\rm maj} \lesssim 28''$ follows an exponential profile, suggesting a disk structure that is presumably dominated by the primary progenitor of this merging system. The best-fit exponential profile for the disk-dominated radial range is overplotted as a blue straight line in Figure 3. To make an estimate of the respective stellar luminosities of the primary and secondary galaxies of the merging system, we assume that the region within $R_{\rm maj} = 28''$ is contributed exclusively by the primary, while the region beyond has significant contribution from both the primary and secondary. The total luminosity of the primary is a sum of the luminosity directly measured in the images within $R_{\rm maj} = 28''$ and an exponential extrapolation beyond by using the average ELLIPSE geometric parameters at $26'' < R_{\rm maj} < 28''$. The luminosity of the secondary is calculated by subtracting the luminosity of the primary from the total luminosity enclosed within the 28.3 mag arcsec^{-2} contour.

The above exercise of decomposing the merging system gives a *g*-band absolute magnitude M_g of -16.28 and a $(g-i)$ color of 0.45 for the primary, and an M_g of -14.39 and a $(g-i)$ color of 0.53 for the secondary. To estimate the stellar mass, we first transform our MegaCam magnitude to the Sloan Digital Sky Survey (SDSS) magnitude using the relation: $(g-i)_{\rm SDSS} = 1.1 \times (g-i)_{\rm MegaCam}$ and $i_{\rm SDSS} = i_{\rm MegaCam} + 0.005 \times (g-i)_{\rm MegaCam}$,[13] and then obtain mass-to-light ratios using the color–mass-to-light relation calibrated for Local

[13] The relations are derived based on the best-fit stellar population models for Local Group dwarf galaxies presented in Zhang et al. (2017).

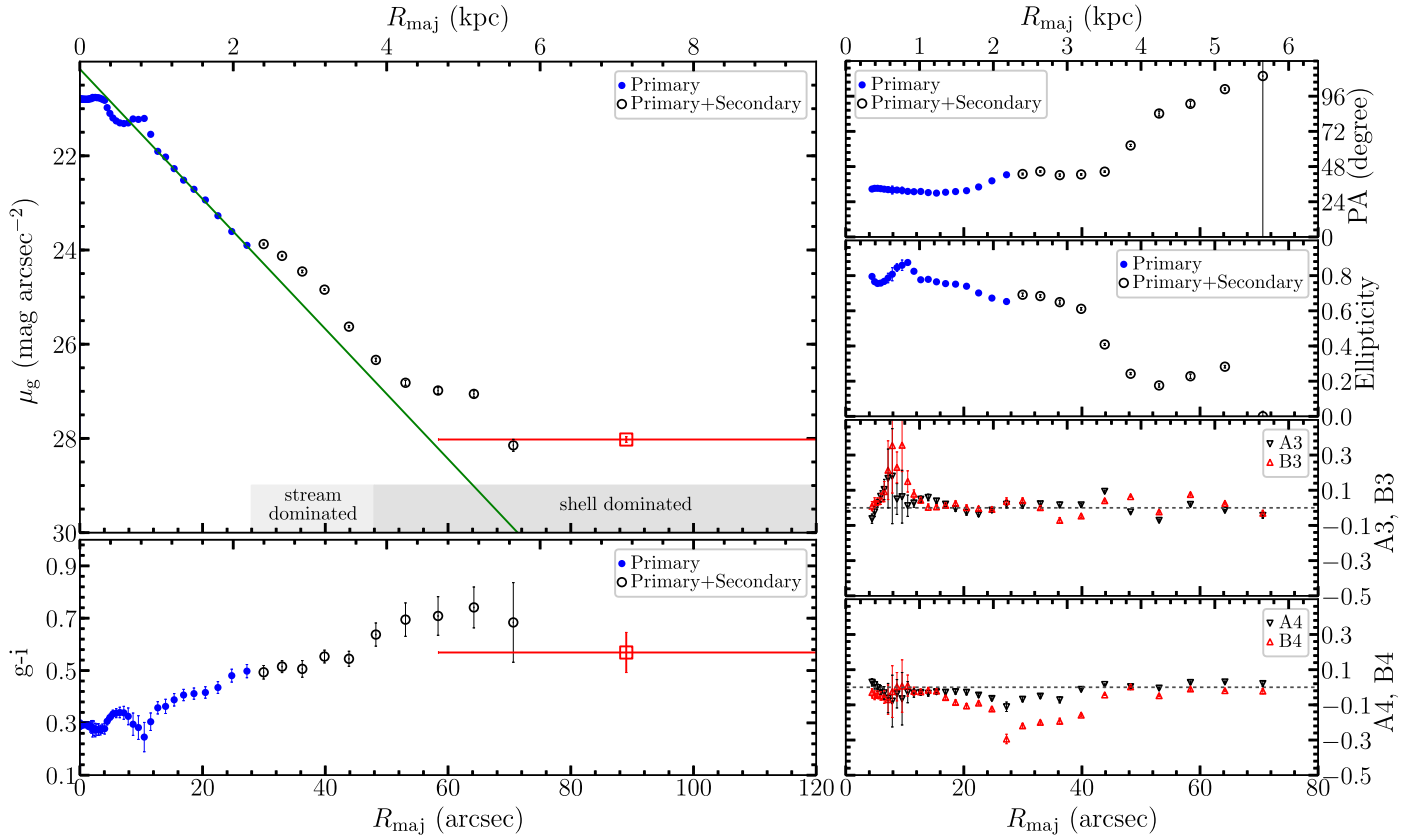

Figure 3. Results of ELLIPSE surface photometry of VCC 848. The upper left panel shows the g-band surface brightness profile, and the lower left panel shows the $(g - i)$ color profile. Radial variations of other ELLIPSE isophote parameters are shown in the right panels. When plotting the surface brightness, color, PA, and ellipticity profiles, the inner radial ranges that are dominated by the primary galaxy are plotted as blue filled circles, while the outer radial ranges with a significant contribution from both the primary and secondary are plotted as black open circles. The red open squares in the left panels represent the photometry for the irregular region enclosed by the 27.3 and 28.3 mag arcsec^{-2} g-band contour levels as marked in Figure 2.

Group dwarf galaxies by Zhang et al. (2017) based on the Flexible Stellar Population Synthesis (FSPS) stellar population models (Conroy et al. 2009). The resultant stellar masses are 1.7×10^8 $M_\odot$ and 3.8×10^7 $M_\odot$ for the primary and secondary, respectively, leading to a 4.5: 1 primary-to-secondary stellar mass ratio. By adopting the stellar-to-dark matter halo mass relation from Guo et al. (2010), the corresponding dark matter halo masses for the primary and secondary are 5.6×10^{10} and 3.4×10^{10} $M_\odot$, respectively, giving a halo mass ratio of 1.6:1. The mass ratio estimated here is likely an upper limit if allowing for a nonnegligible contribution of the secondary to the central exponential part of the system.

The fact that we observe mostly extended stellar shells, rather than tidal tails, around the merging system favors a nearly radial encounter (Quinn 1984). The overall alignment of the stellar shells suggests that the collision was largely along the east–west direction. Because we do not see any distinct stellar concentrations other than the main body, the secondary progenitor has been almost entirely disrupted, leaving behind the observed stellar shells.

4. Star Clusters and Their Implications for Star Formation History

4.1. Detection and Aperture Photometry

We use SExtractor (Bertin & Arnouts 1996) to detect star cluster candidates in the original i-band image, which has the highest spatial resolution among our images. Ordinary star clusters ($r_{\rm eff} \sim 2-10$ pc; e.g., Portegies Zwart et al. 2010) at the distance of VCC 848 are expected to be pointlike or marginally resolved sources at our i-band resolution (e.g., Durrell et al. 2014). We run SExtractor with a BACK_SIZE parameter of 9 pixels and a detection threshold of 3 times the rms noise. A total of 1994 sources are detected in a $7\farcm2 \times 11\farcm2$ cutout image centered around VCC 848. By following the routine procedure of completeness estimation based on artificial star tests (e.g., Munoz et al. 2014), we find that our detection reaches a 90% completeness limit at $i = 23.5$ mag. 1078 of the 1994 sources have $i \leqslant 23.5$ mag.

We perform i-band aperture photometry for the detected sources with a 5 pixel ($0\farcs93$) diameter aperture size. The aperture size is chosen to contain more than half of the total flux expected for a point source and at the same time to reduce as much as possible the contamination from neighboring sources. Local background for each source is determined using a 4 pixel wide background annulus, with an inner radius of 6 pixels. We apply a multiplicative correction factor of 1.8 to the background-subtracted aperture photometry to recover the expected total flux for i-band point sources. To determine the colors, we smooth the g, i, z images to match the u-band spatial resolution, and follow the same procedure described above to obtain u, g, i, z photometry based on the resolution-matched images.

4.2. Selection of Star Cluster Candidates in VCC 848

We select star cluster candidates taking advantage of both the shape and color information. In particular, we use the

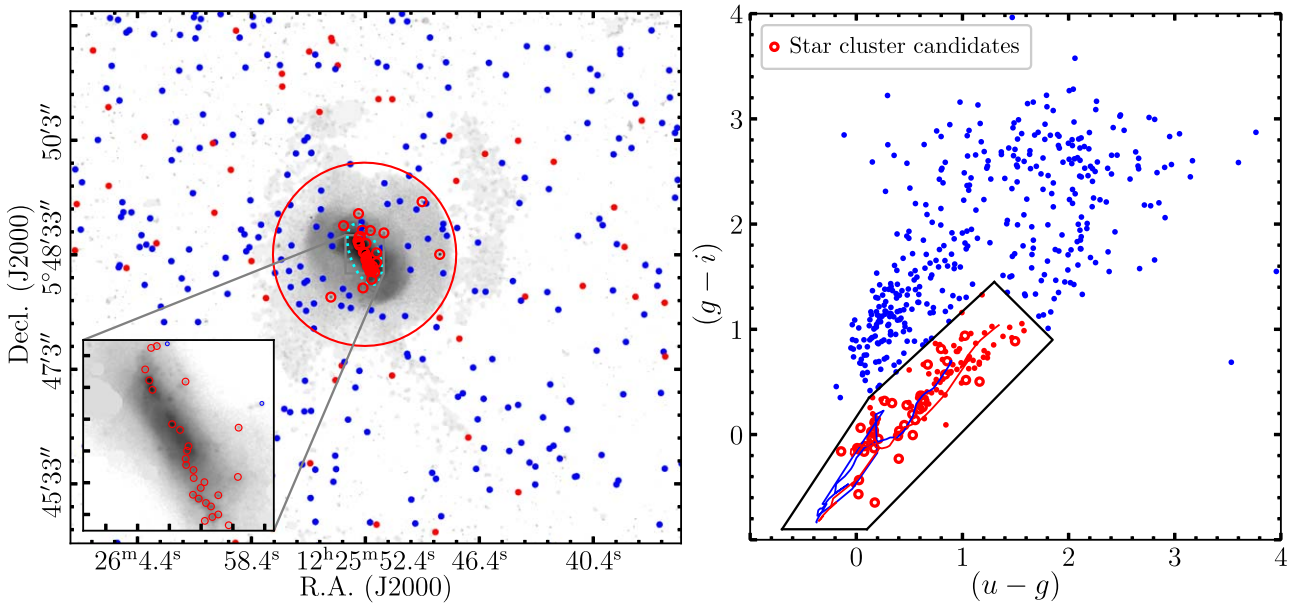

Figure 4. Star cluster candidates with $i < 23.5$ mag detected in the VCC 848 field. The left panel shows the central $7' \times 8'$ of the adaptively smoothed g-band image, and the inset figure to the bottom left is the central $30'' \times 30''$ of the original i-band image. The blue dots represent the point or marginally resolved sources selected based on i-band shape parameters (see the text for details), the red dots represent the point or marginally resolved sources that fall within a $(u - g)$ vs. $(g - i)$ parameter space occupied by star clusters, as delineated by a closed black polygon in the right panel, and the small red open circles represent our final sample of 37 star cluster candidates that satisfy the shape and color criteria and are also within a $1\farcm2$ radius circular region around VCC 848 (big red circle in the left panel). For comparison purposes, the FSPS single stellar population models of $\log(Z/Z_\odot) = -1.98$ and -0.39 (ages from 0.3 Myr to 15 Gyr; Conroy et al. 2009) are overplotted as blue and red curves, respectively, in the right panel. The cyan dotted ellipse in the left panel marks the area used for completeness estimates.

criteria of ELLIPTICITY < 0.2 and FWHM < 4.5 pixels to pick out pointlike or marginally resolved objects with $i < 23.5$ mag. The SExtractor shape parameter measurements are subject to large uncertainties in regions with a steep background gradient, so we relax the requirement for shape parameters if a source in question is spatially coincident with an H II region visible in the Hα image of Gil de Paz et al. (2003). The above selection criteria leave us with 526 sources to be considered for further selection with colors.

The right panel of Figure 4 shows the $(u - g)$ versus $(g - i)$ distribution of the above-selected 526 sources. The sources occupy two distinct branches. The upper branch is identified to be background galaxies, while the lower branch is largely occupied by star clusters and foreground stars. We draw a polygon to delineate a region in the color–color space to single out the most probable star cluster candidates (116 in total). Last, we require that the VCC 848 star cluster candidates be located within a $1\farcm2$ radius circular region, approximately matching the area enclosed by the 27.3 mag arcsec^{-2} g-band brightness contour. This last step leaves us with a final sample of 37 star cluster candidates.

The average number density of the 79 (116–37) color-selected candidates located outside of the $1\farcm2$ radius circular region around VCC 848 is $\simeq 1.0$ arcmin^{-2}. Therefore, we expect an average of $\simeq 4.5$ contaminants for the $1\farcm2$ radius circular region, giving a $\simeq 88\%$ purity for our star cluster sample. We note, however, that 33 of the 37 candidates are concentrated within the central $30''$, implying a 98% purity.

4.3. Stellar Population Modeling

We estimate stellar ages and masses of our star cluster candidates by fitting the FSPS SSP models to u, g, i, z photometry. Considering the age–metallicity degeneracies, we perform two sets of extinction-free stellar population fitting. One imposes a Gaussian prior constraint on metallicities, with a mean of -0.88 dex (chosen to be 0.2 dex lower than the abundance measurements for H II regions by Vilchez & Iglesias-Paramo 2003) and a standard deviation of 0.3 dex, while the other one does not impose prior constraints on metallicities. An upper limit of one-third solar metallicity is adopted for both sets of fitting. We will show that the two sets of spectral energy distribution (SED) fitting give statistically similar age–metallicity distributions. With the best-fit age and metallicity of each cluster, we infer the stellar mass at birth by correcting the present-day mass for mass loss due to stellar evolution, based on the FSPS models. As we will show in Figure 5(c), mass loss caused by dynamical evaporation is not expected to be important for our cluster sample.

4.4. Age–Mass Relation and Its Implication for Star Formation History of VCC 848

The stellar masses at birth are plotted against ages of our star cluster candidates in Figure 5(c). The lower limit of cluster mass increases with age, which is jointly driven by the luminosity-limited detection efficiency, evolutionary fading, and dynamical evaporation. The maximum cluster mass also varies with age, which may be driven by the size-of-sample effect, a time-dependent cluster formation rate (CFR), or cluster mass function (CMF). CMF of young star clusters observed in nearby galaxies can always be described by a power-law $dN/dM \propto M^\alpha$, where $\alpha \simeq -2 \pm 0.2$ (see Krumholz et al. 2019 and references therein). For a constant CFR and $\alpha = -2$ power-law CMF, the maximum cluster mass per logarithmic time interval scales linearly with age due to the size-of-sample effect (e.g., Hunter et al. 2003). Such a linear $M-$age relation is illustrated in Figure 5(c).

Given that dynamical evaporation and tidal shocking are not expected to significantly influence star clusters with $M_\star > 10^5\,M_\odot$

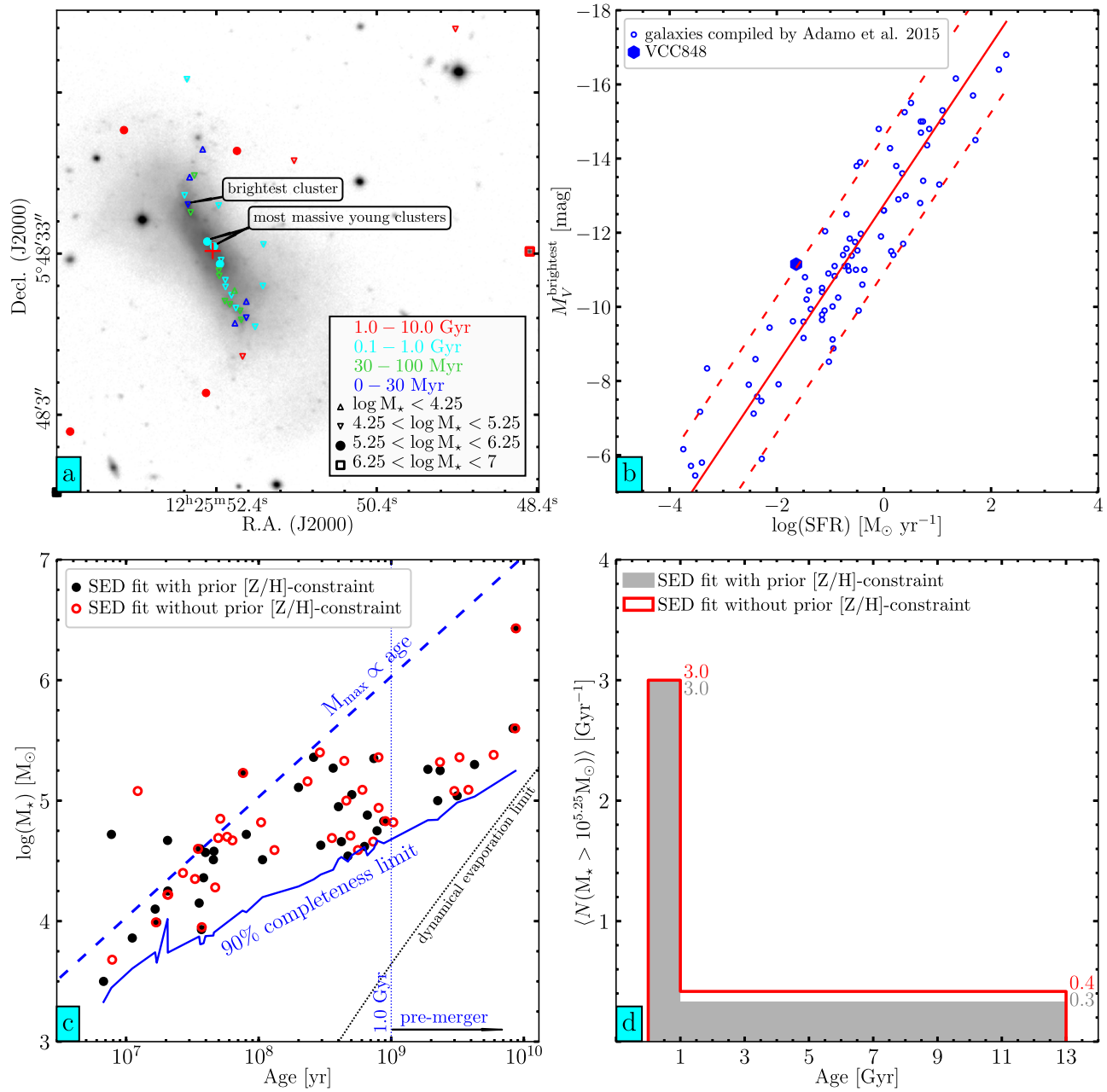

Figure 5. (a) Spatial distribution of the 37 star cluster candidates in VCC 848. (b) The absolute magnitude of the brightest young star cluster is plotted against the SFR of its host galaxy. The blue open circles are nearby galaxies compiled by Adamo et al. (2015), and the blue filled hexagon represents VCC 848. The red solid line is the best-fit linear relation ($M_V^{\rm brightest} = -2.16\log({\rm SFR}) + 12.76$) obtained with the orthogonal distance regression method, and the red dashed lines mark the $\pm 3\sigma$ vertical scatter around the best-fit relation. (c) Age–mass diagram of star cluster candidates in VCC 848. The masses are stellar masses at birth. The results from stellar population fitting with a Gaussian prior constraint on metallicities are shown as filled black circles, while the results from fitting without prior constraint on metallicities are shown as red open circles. The 90% completeness limit of stellar mass is plotted as a blue solid curve. The linear relation between maximum cluster mass and age expected from the size-of-sample effect, together with a constant cluster formation rate and a canonical cluster mass function of $dN/dM \propto M^{-2}$, is plotted as a blue dashed line, which is arbitrarily shifted to match the overall upper mass envelope at intermediate ages. The black tilted dotted line represents the cluster dissolution limit given by Baumgardt & Makino (2003) for a fiducial galactocentric radius of 0.5 kpc and galaxy rotation velocity of 40 km s^{-1}. (d) Average formation rate (Gyr^{-1}) of star clusters with birth mass $M_\star > 10^{5.25}\ M_\odot$ over the age intervals of 0–1 Gyr and 1–13 Gyr.

(Reina-Campos et al. 2018), the CFR of VCC 848 has been significantly enhanced during the past ∼1.0 Gyr, because the observed maximum cluster masses above $10^5\ M_\odot$ do not rise steadily with lookback time, which would otherwise be expected for the size-of-sample effect. However, during the last ∼20–30 Myr, the CFR appears to have started declining. The brightest star cluster of VCC 848, with a V-band absolute magnitude $M_V^{\rm brightest} = -11.15$ mag (derived based on the best-fit model SED), is $>3\sigma$ above the average $M_V^{\rm brightest}$–SFR relation for nearby galaxies (Figure 5(b)), in line with a recent decline of SFR (Bastian 2008).

Our cluster sample is $\gtrsim$90% complete at $M_\star \geqslant 10^{5.25}\ M_\odot$ across nearly the whole age range. Figure 5(d) shows the average number of clusters with $M_\star > 10^{5.25}\ M_\odot$ over age intervals of 0−1 Gyr and 1−13 Gyr. The average CFR in the last 1 Gyr is ∼7–10 times that at earlier times. If the mass

fraction of stars born in star clusters is independent of SFR, as suggested by recent studies (e.g., Chandar et al. 2017), the trend for CFR would be approximately equivalent to that for SFR.

4.5. Spatial Distribution

The two most massive young star clusters (<1 Gyr), which have ages $\gtrsim$0.3 Gyr and $M_\star \simeq 10^{5.4}\ M_\odot$, are near the galactic center, while the youngest star clusters ($\lesssim$30 Myr), which have $M_\star < 10^{5.0}\ M_\odot$, are at large distances ($\geqslant 10''$) from the center (Figure 5(a)). This suggests that the most intense merging-induced star formation happened near the galactic center a few hundred Myr ago, after which active star-forming activities have shifted to larger radii. Star clusters with ages >1 Gyr appear to avoid the central disk region and might be regarded as (globular) clusters formed in the progenitor galaxies.

5. Summary and Discussion

We present the first study of a gas-dominated BCD galaxy (VCC 848) that hosts extended stellar shells and thus is confirmed to be a dwarf–dwarf merger. The stellar light distribution implies a nearly radial encounter between the progenitor galaxies. Our isophotal analysis implies a primary-to-secondary stellar mass ratio $\lesssim$5 and a corresponding dark matter halo mass ratio $\lesssim$2 for this advanced major merger. We use the age–mass distribution of photometrically selected star cluster candidates to probe the CFR, and find that the average CFR in the past ~1 Gyr, which is comparable to the timescales expected for dwarf merging events (e.g., Bekki 2008), was enhanced by a factor of ~7–10.

The period of the most intense merging-induced starburst, which was concentrated near the galactic center a few hundred Myr ago, is expected to be over by now, because the secondary progenitor has been almost entirely disrupted. The current star formation activities traced by the youngest star clusters mainly occur at large galactocentric distances ($\gtrsim$1 kpc). The overall trend of the temporal and spatial variation of star formation activities in VCC 848 is in general agreement with the Bekki (2008) simulations. In a companion paper, we will present interferometric observations of the H I gas and numerical simulations in order to gain further insight into this unique merging system.

H.X.Z. acknowledges support from the National Key R&D Program of China (2017YFA0402702), the NSFC grant (Nos. 11421303 and 11973039), and the CAS Pioneer Hundred Talents Program. S.P. acknowledges support from the New Researcher Program (Shinjin grant No. 2019R1C1C1009600) through the National Research Foundation of Korea.

ORCID iDs

Hong-Xin Zhang https://orcid.org/0000-0003-1632-2541
Sanjaya Paudel https://orcid.org/0000-0003-2922-6866
Rory Smith https://orcid.org/0000-0001-5303-6830
Thomas H. Puzia https://orcid.org/0000-0003-0350-7061
Eric W. Peng https://orcid.org/0000-0002-2073-2781
Laura Ferrarese https://orcid.org/0000-0002-8224-1128
Alessandro Boselli https://orcid.org/0000-0002-9795-6433
Se-Heon Oh https://orcid.org/0000-0002-5648-9920

References

Adamo, A., Kruijssen, J. M. D., Bastian, N., Silva-Villa, E., & Ryon, J. 2015, MNRAS, 452, 246
Amorisco, N. C., Evans, N. W., & van de Ven, G. 2014, Natur, 507, 335
Annibali, F., Nipoti, C., Ciotti, L., et al. 2016, ApJL, 826, 27
Bastian, N. 2008, MNRAS, 390, 759
Baumgardt, H., & Makino, J. 2003, MNRAS, 340, 227
Bekki, K. 2008, MNRAS, 388, L10
Bertin, E., & Arnouts, S. 1996, A&AS, 117, 393
Binggeli, B., Sandage, A., & Tammann, G. A. 1985, AJ, 90, 1681
Binggeli, B., Tammann, G. A., & Sandage, A. 1987, AJ, 94, 251
Blakeslee, J. P., Jordan, A., Mei, S., et al. 2009, ApJ, 694, 556
Catalan-Torrecilla, C., Gil de Paz, A., Castillo-Morales, A., et al. 2015, A&A, 584, 87
Chandar, R., Fall, S. M., Whitmore, B. C., & Mulia, A. J. 2017, ApJ, 849, 128
Chilingarian, I. V. 2009, MNRAS, 394, 1229
Cicuendez, L., & Battaglia, G. 2018, MNRAS, 480, 251
Conroy, C., Gunn, J. E., & White, M. 2009, ApJ, 699, 486
Durrell, P. R., Cote, P., Peng, E. W., et al. 2014, ApJ, 794, 103
Ferrarese, L., Côté, P., Cuillandre, J.-C., et al. 2012, ApJS, 200, 4
Gil de Paz, A., Madore, B. F., & Pevunova, O. 2003, ApJS, 147, 29
Grossi, M., Hunt, L. K., Madden, S. C., et al. 2015, A&A, 574, 126
Guo, Q., White, S., Li, C., & Boylan-Kolchin, M. 2010, MNRAS, 404, 1111
Haynes, M. P., & Giovanelli, R. 1984, AJ, 89, 758
Haynes, M. P., Giovanelli, R., Martin, A. M., et al. 2011, AJ, 142, 170
Hernquist, L., & Quinn, P. J. 1988, ApJ, 331, 682
Hernquist, L., & Spergel, D. N. 1992, ApJL, 399, 117
Hunter, D. A., Elmegreen, B. G., Dupuy, T. J., & Mortonson, M. 2003, AJ, 126, 1836
Johnston, E. J., Eigenthaler, P., Puzia, T. H., et al. 2019, ApJ, 873, 1
Kravtsov, A. V. 2013, ApJL, 764, 31
Krumholz, M. R., McKee, C. F., & Bland-Hawthorn, J. 2019, ARA&A, 57, 227
Makarova, L. N., Makarov, D. I., Antipova, A. V., Karachentsev, I. D., & Tully, R. B. 2018, MNRAS, 474, 3221
Munoz, R. P., Puzia, T. H., Lancon, A., et al. 2014, ApJS, 210, 4
Naab, T., & Ostriker, J. P. 2017, ARA&A, 55, 59
Paudel, S., & Sengupta, C. 2017, ApJL, 849, L28
Paudel, S., Sengupta, C., & Yoon, S.-J. 2018a, AJ, 156, 166
Paudel, S., Smith, R., Duc, Pierre-Alain, et al. 2017, ApJ, 834, 66
Paudel, S., Smith, R., Jin Yoon, S., Calderon-Castillo, P., & Duc, P.-A. 2018b, ApJS, 237, 36
Pearson, W., Besla, G., Putman, M. E., et al. 2016, MNRAS, 459, 1827
Portegies Zwart, S. F., McMillan, S. L. W., & Gieles, M. 2010, ARA&A, 48, 431
Privon, G. C., Stierwalt, S., Patton, D. R., et al. 2017, ApJ, 846, 74
Quinn, P. J. 1984, ApJ, 279, 596
Reina-Campos, M., Kruijssen, J. M., Pfeffer, J., et al. 2018, MNRAS, 481, 2851
Schlafly, E. F., & Finkbeiner, D. P. 2011, ApJ, 737, 103
Shin, K., Ly, C., Malkan, M. A., et al. 2019, arXiv:1910.10735
Stierwalt, S., Besla, G., Patton, D., et al. 2015, ApJ, 805, 2
Vilchez, J. M., & Iglesias-Paramo, J. 2003, ApJS, 145, 225
Zhang, H.-X., Puzia, T. H., & Weisz, D. R. 2017, ApJS, 233, 13
Zibetti, S., Charlot, S., & Rix, H. 2009, MNRAS, 400, 1181